Earth, Planets and Space

FULL PAPER Open Access

Surface wave imaging using deep reflection seismic data: a study on the Cuonadong dome

Guangwen Wang[1,2], Zhanwu Lu[1,2*], Wenhui Li[1,2], Shuai Xue[1,2], Haiyan Wang[1,2], Yongzhi Cheng[1,2], Si Chen[1,2] and Wei Cai[1,2]

Abstract

As interference waves in deep reflection data processing, surface waves are often suppressed as noise, but surface waves carry considerable underground media information, including structural information and the physical properties of rocks. Reasonable extraction and use of surface wave signals are of great significance when studying shallow characteristics. Deep reflection data are collected using large offsets, trail spacing, and explosive sources. The surface wave energy tends to be stronger, and the high-frequency surface wave signal is abundant. After extraction and inversion, the shallow shear wave velocity structure can be obtained. Near the Cuonadong dome in the southern Tibetan detachment system (STDS), a large number of leucogranites are developed in the core, containing important rare metal minerals and high metallogenic potential. However, studies regarding the shallow structure in this region are rare. In this paper, we use deep reflection data from a profile through the Cuonadong dome to obtain the S-wave velocity structure of the study area by extracting the surface wave fundamental-mode dispersion curve and inversion. Combined with regional geological and magnetotelluric data, we supposed that the thickness of the Cuonadong dome sediment layer (< 1.4 km/s) varies greatly from east to west, the thickness of the sediment layer is the deepest near the Cuona fault and Jisong fault (more than 1 km), and the core of the dome is the thinnest. Under the Cuonadong dome, there are obvious high-velocity anomalies (> 2.2 km/s), and the horizontal S-wave velocity changes greatly, which is mainly related to the destruction of magmatic activity since the Miocene. These understandings of the structure and velocity field of the Cuonadong dome can provide a powerful geophysical basis for establishing the dome structure model and searching for hidden ore bodies.

Keywords: Cuona fault, Deep reflection, Cuonadong dome, Leucogranite, S-wave velocity

*Correspondence: luzhanwu78@163.com

[1] Lithosphere Research Center, Institute of Geology, Chinese Academy of Geological Sciences, 26 Baiwanzhuang street, Xicheng District, Beijing 100037, China
Full list of author information is available at the end of the article

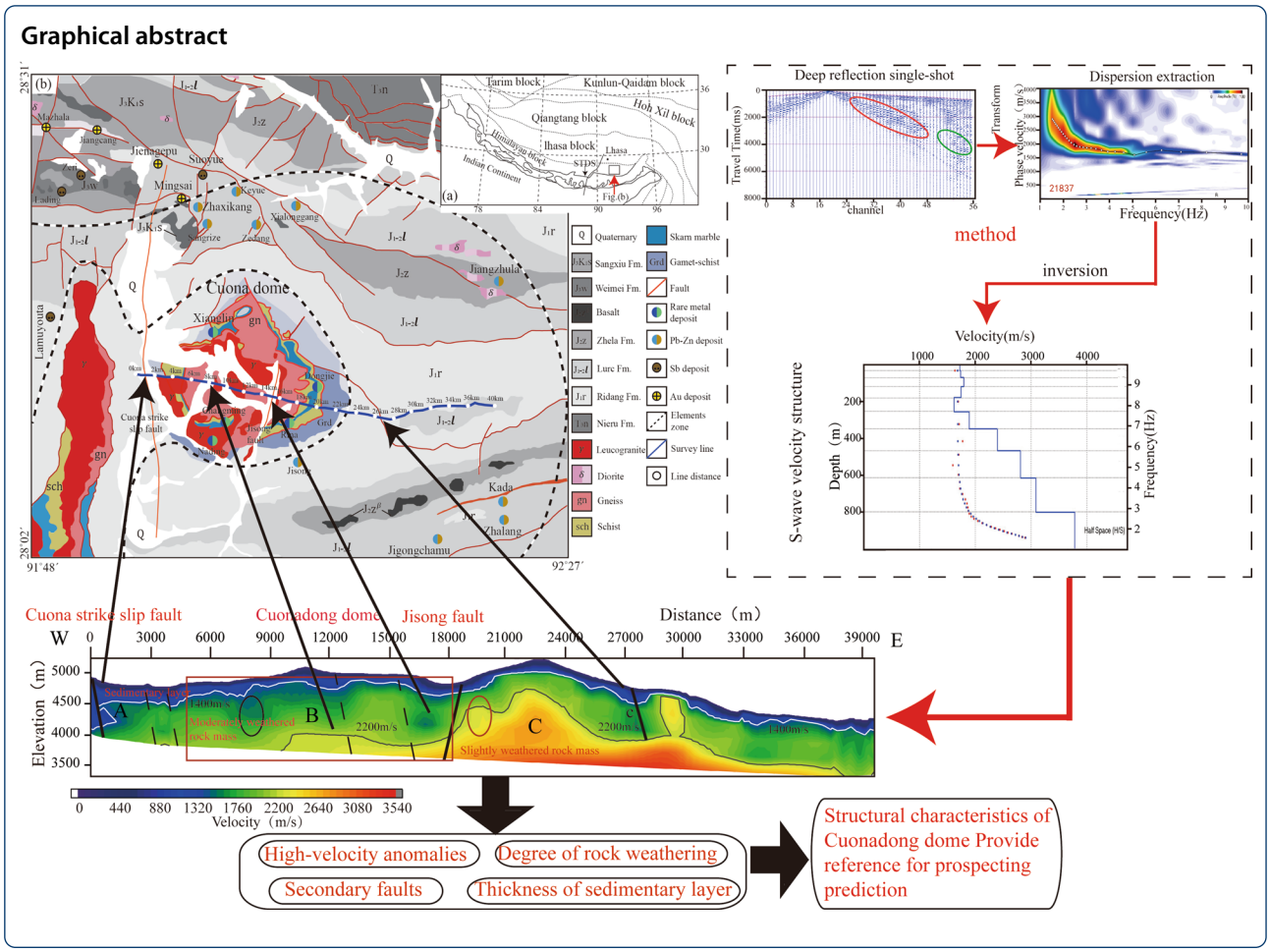

Introduction

Surface waves, as strong-amplitude, low-frequency linear interference waves, are often suppressed by various combinations of filtering in deep reflection seismic data processing. However, surface waves carry considerable underground media information on structures, physical rock properties, and fluids. Therefore, the reasonable use of surface wave signals can obtain S-wave velocities in shallow subsurfaces, which is important for studying shallow tectonic features and mineralization (Feng et al. 2019; Zhang et al. 2020). With the emergence of high-precision seismic instruments and improvements in surface wave technology, surface wave imaging has become a research focus for many scholars in recent years. Deep reflection seismic data often have strong surface wave signals in single-shot records due to acquisition methods with large offsets, strong energy, and trail spacing, especially in high-frequency signals of 1–10 Hz, which can be used to study fine structures in shallow subsurfaces (Xie et al. 2021).

The Cuonadong dome is located in the Tethys Himalayan orogenic belt close to the southern Tibetan detachment system (STDS). The interior of the dome contains a large number of leucogranites surrounded by sandstones, slates, marls, and other important mineralized rocks, and the metallogenic potential is enormous (Zhou et al. 2014; Lin et al. 2016; Guo et al. 2019a; b). At present, many tungsten, tin, and beryllium deposits have been found around the Cuonadong dome (Fu et al. 2017; 2018a; 2020b; Huang et al. 2018; Shi et al. 2020). The former Ministry of Land and Resources, China, designated the Zhaxikang mining area and the surrounding Cuonadong dome as national integrated exploration areas (Blisniuk et al. 2001; He et al. 2020; Li et al. 2016, 2017b, 2020a). However, studies on the Cuonadong dome are mostly based on geochemistry and structural geology, and there is relatively little geophysical information, especially shallow geophysical information, which is crucial to constrain the tectonic features of the dome and study the characteristics of faults and sedimentary layers. This shallow information can provide corresponding

geophysical evidence for mineralization and mineral searches (Li et al. 2017a; Fan et al. 2019; Jiao et al. 2016, 2019).

In this paper, we use an east–west trending deep seismic reflection profile across the Cuonadong dome to extract the surface wave signal. After preprocessing, dispersion extraction, inversion, and other steps, we obtain the S-wave velocity structural characteristics of the dome surface (approximately 1.0 km). Combined with geological surface data and magnetotelluric data, we obtain the relationship between the thickness changes in the sedimentary layer of the Cuonadong dome, the fluctuation characteristics of the bedrock interface, the location and extension of the hidden faults, and the changes in the velocity of the dome structure and metal deposit (Beaumont et al. 2001; Liu et al. 2021).

Geological background

The northern Himalayan tectonic belt is located in the southern Yajiang suture zone (ITSZ) and northern STDS. It is located in the middle and eastern parts of the Himalayan Tethys orogeny and has experienced long-term sedimentary–structural evolution since the Pan-African movement on the northern margin of Gondwanan land. In particular, it has been subjected to the expansion, reduction, and closure of the Yarlung Zangbo ocean basin since the Triassic, as well as the strong collisional orogen and large-scale compression and extension between the Himalayan block and the Gangdise block (Chen et al. 1990; Lee et al. 2004; Wang et al. 2012; Dong et al. 2018; Li et al. 2020b; Li et al. 2020a). Multiple dome structures have been formed (Fig. 1a). Among them, the Cuonadong dome is located in the eastern part of the Himalayan dome belt in the Tethyan, approximately 40 km southeast of the Yalaxiangbo dome, and approximately 23 km north of the southern Tibetan detachment system. The dome is close to the Cuona Rift, its geographical location is relatively special (Cao et al. 2020), and it mainly contains Paleozoic, Triassic, Jurassic, Cretaceous, Quaternary, and other stratigraphic units. Magmatic rocks are widely distributed, mainly in the Mesozoic and Cenozoic. The representative acidic

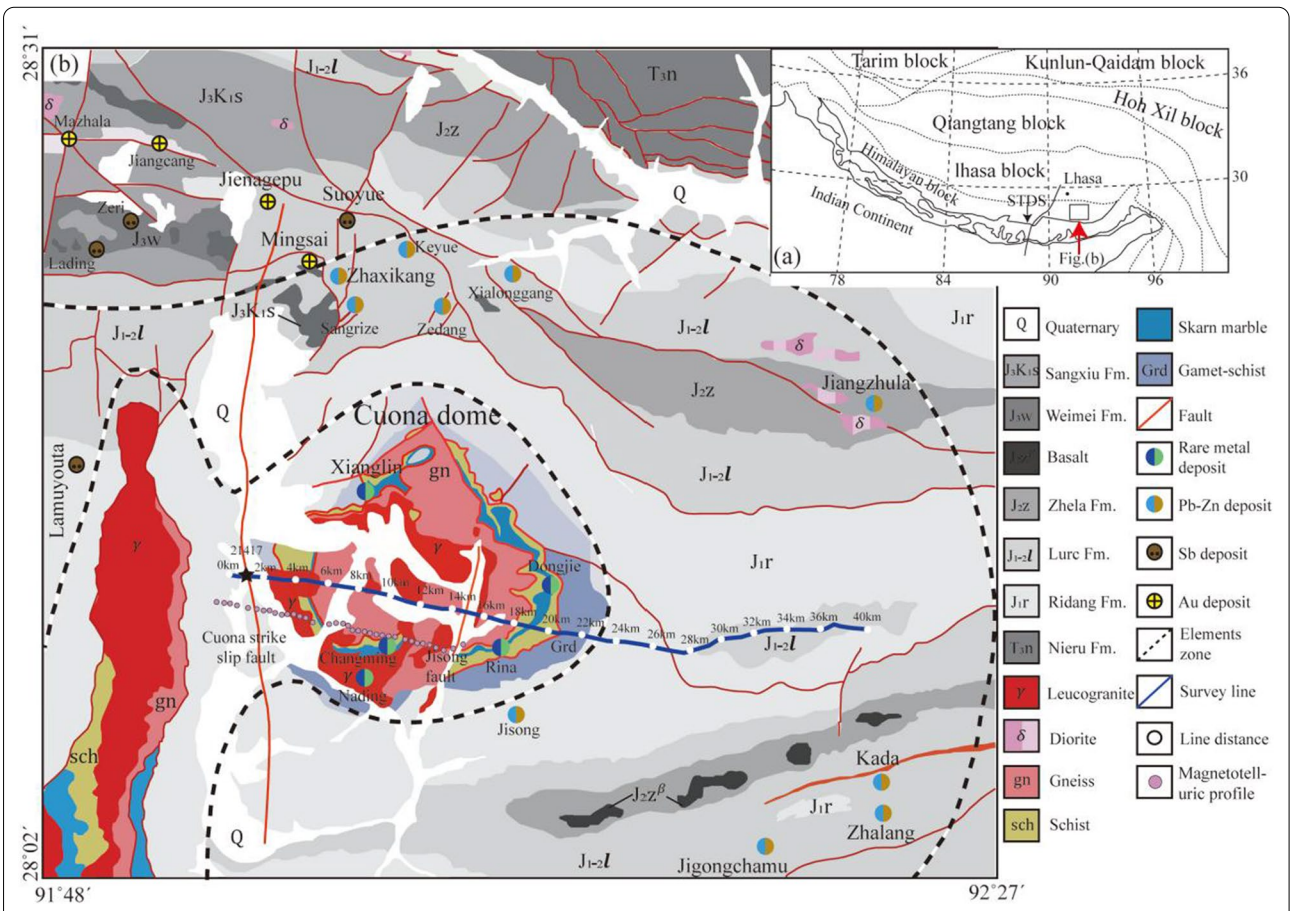

Fig. 1 **a** Sketch map of the Tibetan Plateau and its surrounding terranes. **b** Geologic and ore deposit distribution map of the Zhaxikang Pb–Zn polymetallic ore-concentration area (modified from Liang et al. 2021)

intrusive rocks are Cuonadong leucogranites, and the basic intrusive rocks are mainly Early Cretaceous dyke intrusions. In addition to Quaternary sediments, the rest of the strata have undergone different degrees and different periods of metamorphism, forming different metamorphic rock types and different metamorphic facies belts, mostly slate, schist, and metamorphic sandstone.

Due to the collision and extrusion of the Indian plate and the Asian–European plate, a large number of detachment faults appear around the Cuonadong dome. The underground thermal material gushes up through the detachment fault and interacts with the surrounding rock mass, providing conditions for the formation of polymetallic deposits (Wang et al. 2010; Yang et al. 2011; Fu et al. 2018b; 2020a). In recent years, tungsten, tin, and beryllium mineralization clues have been found in the Cuonadong dome located in the contact zone between granite and Jurassic surrounding rock (Fig. 1b) (Zhang et al. 2017; Xie et al. 2017, 2018, 2019; Jiao et al. 2020).

Data processing

Data acquisition

The geological structure around the Cuonadong dome is complex and includes multiple structural areas (STDS, Dongga syncline, Naji anticline, Cuonadong dome) and mining areas (Zhaxikang mining area, Mingsai mining area, Suoyue mining area). To study the deep geophysical characteristics and metallogenic background of the Cuonadong dome, the Institute of Geology, Chinese Academy of Geosciences, set a deep reflection profile across the Cuonadong dome (Fig. 1). The profile, which is approximately 40 km, crosses the core and the sides of the dome. The strata crossed mainly include Quaternary, Jurassic sandstones, Slates, Leucogranite, and Cambrian gneisses.

A total of 183 single-shot points were collected from deep reflection profiles, with specific acquisition parameters, as shown in Table 1. In the raw data (Fig. 2), surface waves are relatively developed, especially the near-offset surface wave signal (red circle), showing regular linear characteristics with strong energy. The far offset (green circle) can also track the surface wave signal. By extracting regular linear surface wave signals, the mapping quality of surface wave dispersion energy can be improved, the reliability of picking up dispersion curves can be enhanced, and the inversion results can be more accurate.

Data analysis

Frequency spectrum analysis

Traditional multichannel surface wave data processing tends to suppress other forms of interference waves to achieve the desired filtering effect while also losing some of the effective signals (Park et al. 1998, 1999; Xia et al. 1999; Ivanov et al. 2005; Li et al. 2022). Spectrum analysis reveals that the surface wave energy is mainly concentrated between 6 and 16 Hz (Fig. 3b). Because deep reflection data acquisition uses explosives as the source, the surface wave energy is relatively strong, and there is basically no interference of other seismic waves in the 0–2 s range of the single-shot record (Fig. 3a). Therefore, we use the original data to preserve the effective signals in different frequency ranges of the surface waves by intercepting the data and extracting the dispersion curves. The total length of the deep reflection profile is approximately 40 km, the effective frequency range is 1.5–8 Hz, and the phase velocity is basically within 500–3500 m/s. Through screening, we finally use 173 dispersions for inversion.

Analysis of different channel numbers

Deep reflection data acquisition adopts 720-channel reception. Due to surface heterogeneity, it is difficult to accurately assess the underground medium information by directly using 720-channel data. However, when the number of receiving channels is small, it affects the mapping quality of the dispersion energy, which is not conducive to improving the accuracy of dispersion curve extraction. Therefore, we conducted tests to select the

Table 1 Deep reflection seismic data acquisition parameters

Acquisition parameters	
Shot interval	**Small shot 250 m; medium shot 3000 m; large shot 50,000 m**
Trace interval	50 m
Sampling rate	2 ms
Record duration	Medium, small 30 s; large shot 60 s
Offset	Small shot: 14,975 m; medium shot: 22,475 m; large shot: full array
Receiving mode	Medium, small: 720-channel reception; large shot; full array
Instrument types	428 Digital seismograph
Source mode	Explosive source

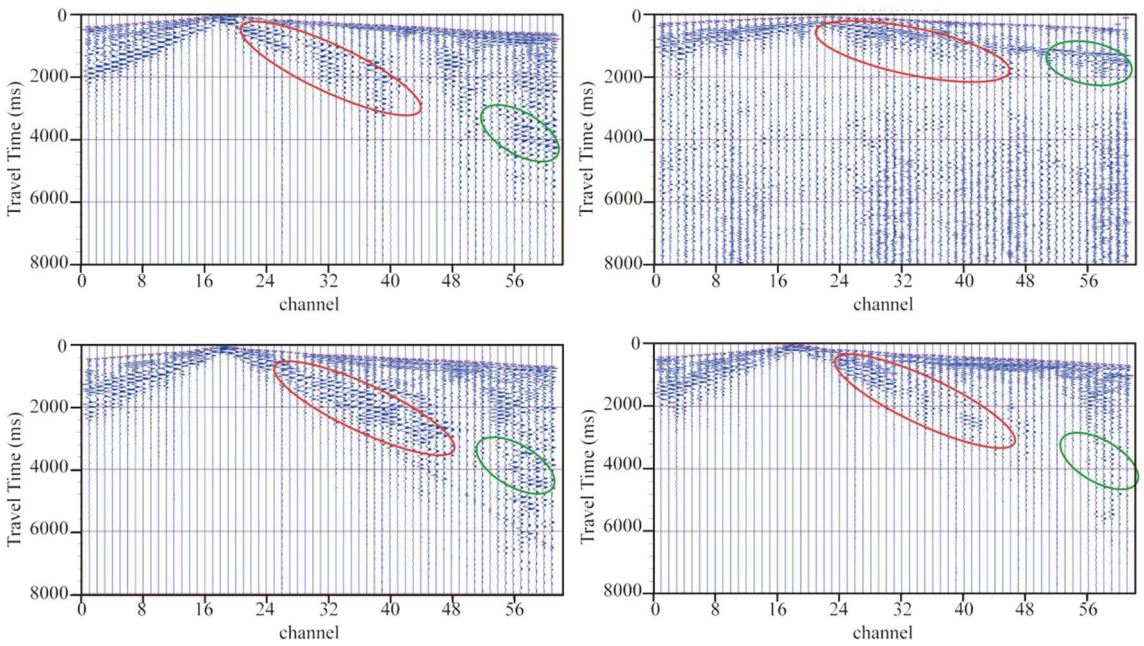

Fig. 2 Original single-shot data (red ellipse is near offset and green ellipse is far offset)

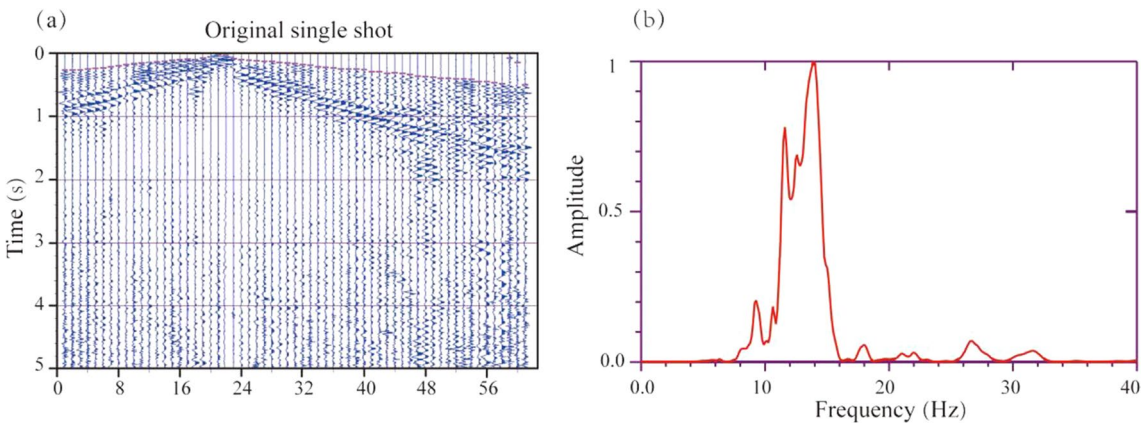

Fig. 3 Original single-shot frequency spectrum. **a** Original single-shot record. **b** Amplitude–frequency graph

most suitable multichannel collection method for data processing. (1) Bilateral 60-channel reception (Fig. 4a): the continuity of the fundamental-mode dispersion curve is better, especially for the low-frequency information, which can be continuously traced, even to 1.5 Hz, and the high-frequency signal is also more developed, which can be traced to 9.5 Hz. (2) Bilateral 40-channel reception (Fig. 4b): the continuity of the fundamental-mode dispersion is significantly reduced, and the low-frequency signal can be traced only to 2 Hz, but the continuity of the high-frequency signal is still better, and higher-order dispersion appears. (3) Unilateral 30-channel reception (Fig. 4c): the energy of the low-frequency part (2–4 Hz) of the fundamental-mode dispersion is weak, but the energy of the high-mode dispersion is strong. It is difficult to accurately identify the dispersion curve in the high-frequency and low-frequency parts. (4) Unilateral 20-channel reception (Fig. 4d): the fundamental mode and the high mode of the low-frequency part are combined, which is difficult to distinguish. Therefore, it is difficult to accurately extract the dispersion curve. Through the comparison of different reception methods and different channels, we adopted 60-channel bilateral reception to extract the dispersion curves. This can improve

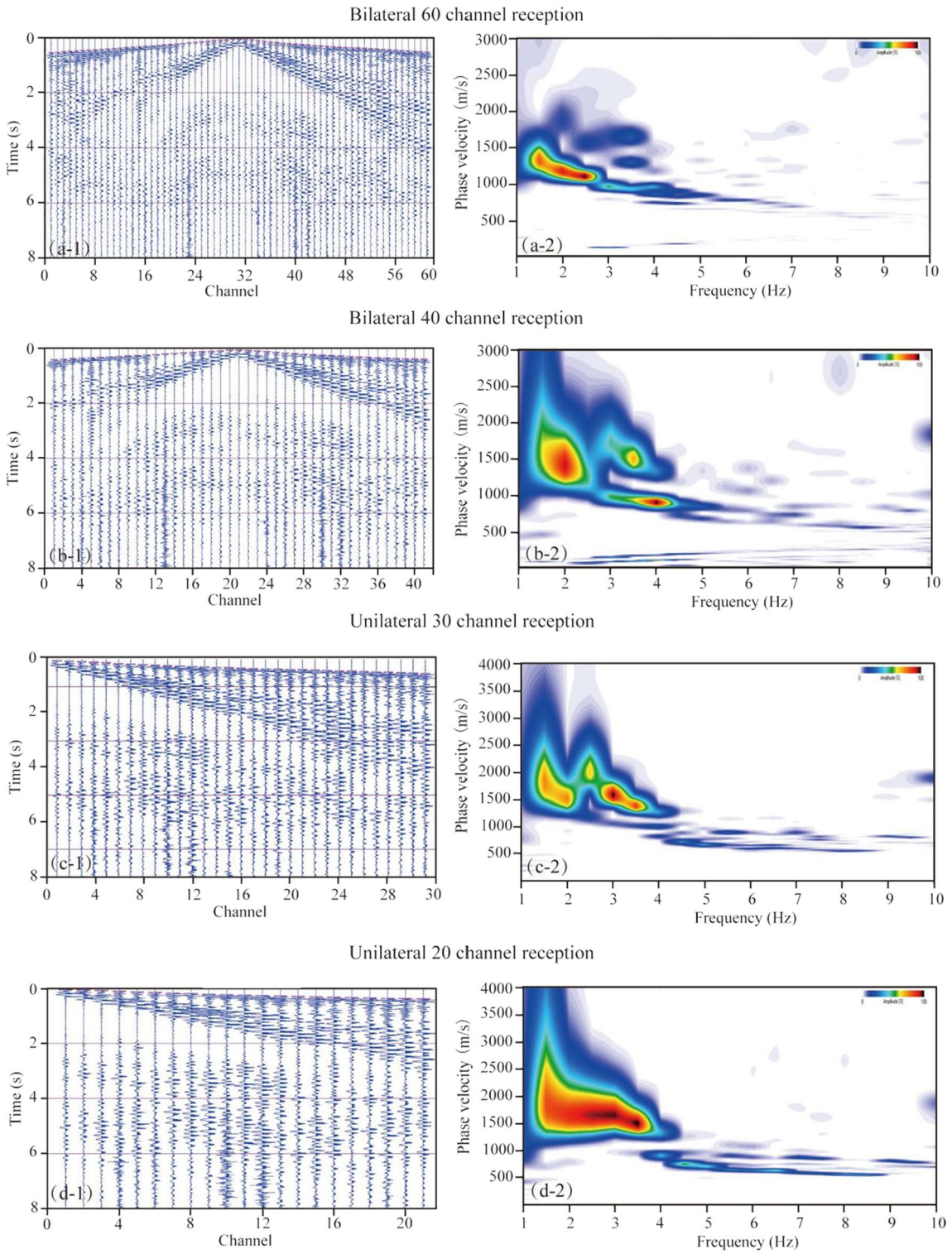

Fig. 4 Dispersion energy diagram of different reception modes. **a** Bilateral 60-channel reception. **b** Bilateral 40-channel reception. **c** Unilateral 30-channel reception. **d** Unilateral 20-channel reception

the accuracy of dispersion extraction and increase the reliability of inversion accuracy.

Surface wave inversion

The surface wave inversion is inseparable in a good initial model. Establishing a suitable initial model can provide better constraints on the inversion of the fundamental surface wave. Because the deep reflection profile across the Cuonadong dome is relatively long and passes through multiple tectonic units and ore-concentration areas, the regional velocity changes drastically, and the initial model is difficult to set. Previous experience shows that the phase velocity of the fundamental Rayleigh surface wave is the most sensitive to the S-wave velocity at a depth of 1/3 of its wavelength. In a uniform half-space Poisson medium, the relationship between the phase velocity and S-wave velocity satisfies the formula $C = 0.92$ Vs. A suitable initial model can be obtained through this relationship, that is, the measured Rayleigh wave phase velocity is divided by 0.92 to obtain the S-wave velocity, the depth is 1/3 of its wavelength, and finally, the average is taken to obtain the initial S-wave velocity model of the study area (Feng et al. 2019).

Surface wave inversion is based on the sensitivity matrix (called a "Jacobian" matrix) that depicts the relative change in phase velocity of the theoretical (modeled) dispersion curve for a unit change in velocity of a particular layer in the model. The dispersion curve of surface waves and underground structures is a complex nonlinear relationship, which is mainly related to parameters such as P-wave velocity, S-wave velocity, density and layer thickness. The sensitivity of surface wave dispersion and S-wave velocity is much higher than that of P-wave velocity and density, followed by layer thickness (Xia et al. 1999, 2015; Feng et al. 2019; Zhang et al. 2020). In this paper, the S-wave velocity and layer thickness are mainly used as the initial model parameters. The profile passes through multiple structural units, and the velocity changes greatly. Therefore, at each measuring point, the initial velocity model is established according to the characteristic that the phase velocity of the Rayleigh wave is the most sensitive to the shear wave velocity at a depth of 1/3 of its wavelength (Feng et al. 2019). According to the principle of "shallow subdivision and deep coarseness", the initial model is divided into 10 layers from shallow to deep (Fig. 5, red line).

Forward simulation

In this part, we mainly use tesseral-2d forward simulation software (Wei et al. 2014). First, the dispersion curve of the original single shot is used to establish the initial velocity model for inversion according to the principle that the surface wave is the most sensitive at 1/3 of the wavelength. The shear wave velocity obtained from inversion is used as the initial model of forward modeling (Fig. 6a). Then, the wave equation is used to simulate the single-shot record (Fig. 6b) and extract the dispersion curve, and the S-wave velocity structure is obtained by inversion. Through comparison, the S-wave velocity is similar in the shallow layer but different in the deep layer (Fig. 6e, f). The main reason is that the original data are affected by the terrain and horizontal heterogeneity, and these effects are mainly reflected in the low-frequency signals. The impact on the high-frequency signals mainly comes from human activities. However, the study area is basically located in the uninhabited plateau and mountainous area, so the interference of the high-frequency signals is weak. Therefore, the S-wave velocity will be different in the low-frequency part but similar in the high-frequency part. Through forward modeling, for establishing the initial model by using the selected dispersion curve, a reasonable selection of the depth in the initial model will directly affect the reliability of the inversion results. Therefore, we analyzed the confidence of different points on the profile and calculated the confidence of inversion results at different depths. From the results (Fig. 7), we found that the confidence is basically more than 80%. The reliability of the results decreases with increasing inversion depth, but it tends to be stable when the depth reaches 1 km. Therefore, it is considered that the inversion depth at 1 km is reliable.

Results and discussion

The S-wave velocity profile reflects the characteristics of the velocity field and tectonic variations in the Cuonadong dome and its adjacent area. We combined geological and magnetotelluric data to interpret the faults, the sedimentary layers, and the degree of lithological weathering of the Cuonadong dome and its adjacent area. We obtained the following points based on the velocity profile.

Characteristics of S-wave velocity in different geological units

By selecting the inversion results at different locations (Fig. 5), we discovered that the S-wave velocity reflected the characteristics of different strata (Point 21433, Point 21695, Point 21837, Point 21837). (1) Point 21433 (Fig. 5a) is located in the Quaternary sedimentary layer close to the Cuona Rift. The sedimentary layer is thicker, and the S-wave velocity is lower. The S-wave velocity indicates that at a position above 200 m underground, the velocity changes greatly, showing a trapezoidal increase, which may be related to the surface sediment and groundwater, and the velocity changes are small below 230 m. (2) Point 21695 (Fig. 5b) is located in the

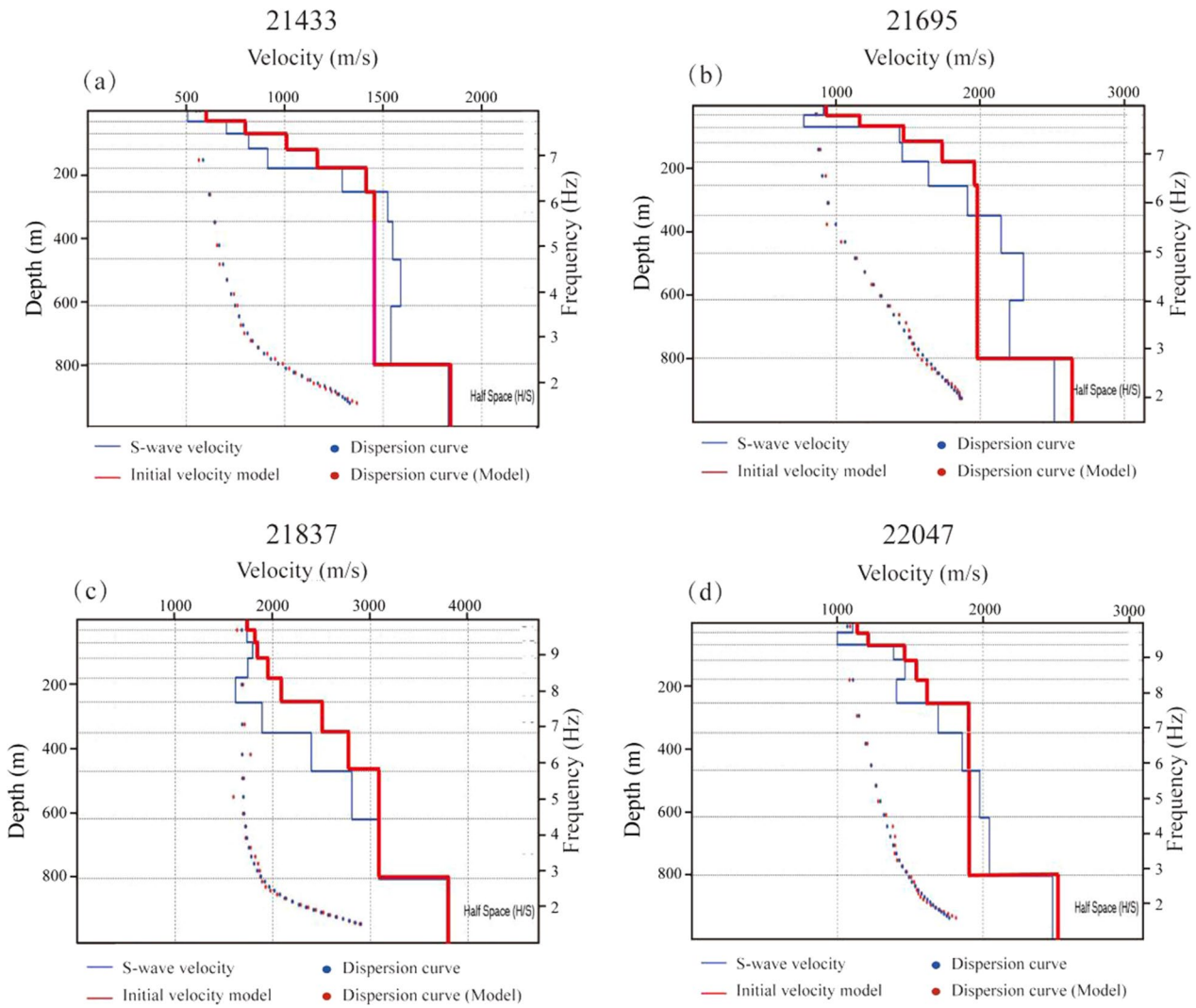

Fig. 5 Inversion results of S-wave velocity at different shot points. Red line is initial velocity. Blue line is inverted S-wave velocity model

core of the Cuonadong dome, and it is mainly composed of leucogranite and metamorphic rocks. The S-wave velocity is generally high, and the minimum velocity is close to 1000 m/s. (3) Point 21837 (Fig. 5c) is located on a rare metal mineralization belt on the edge of the Cuonadong dome, and around this point is mainly sandstone, slate, and schist. The maximum S-wave velocity is close to 4000 m/s. This trend is mainly due to the existence of a metal metallogenic belt, which makes the consolidation and compactness of the rock increase, and the S-wave velocity increases significantly. (4) Point 22,047 (Fig. 5d) is located in the slate and sandstone strata of the Jurassic system. Due to the relatively large degree of surface fragmentation, the shallow velocity is low, but the deep velocity is high.

Stratification characteristics

The Cuonadong dome margin is covered with Quaternary sediments, and the exact thickness of Quaternary sediments has not been studied and detected thus far. The morphology of the rocks beneath the sediments has important reference significance for studies on tectonic movement and mineralization formation. There has been extensive experimental petrology research on the shear wave velocity of different lithologies (Ma et al. 2012; Xu et al. 2012; Chen et al. 2021). For sedimentary and strongly weathered rocks with large natural water contents and a wide range of variations in pore ratios, S-wave velocities generally range from 480 m/s to 1400 m/s (Ma and Lu 2012; Chen et al. 2021). We take 1400 m/s as the interface between the sedimentary layer and the strongly weathered bedrock

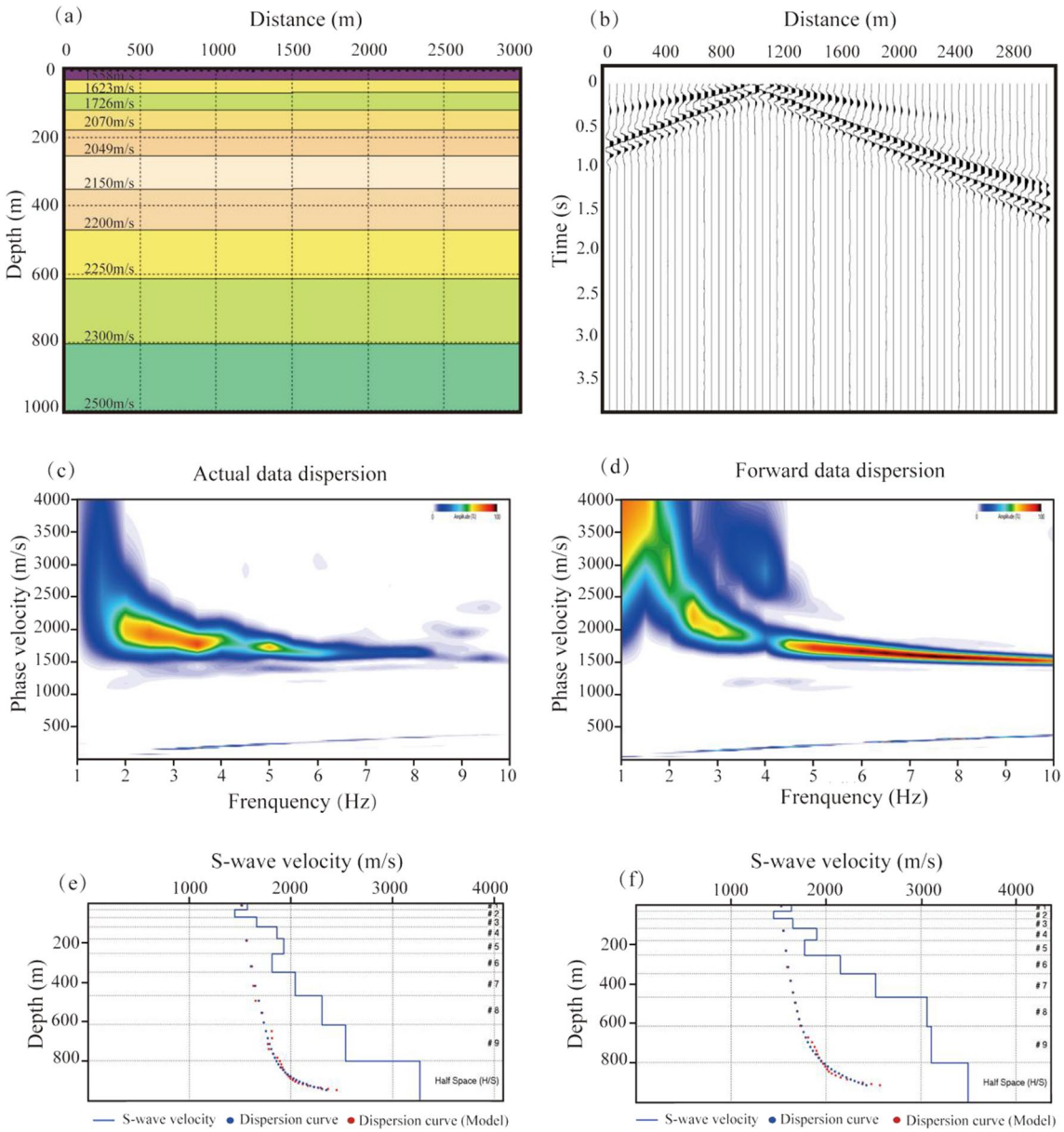

Fig. 6 Comparison between the forward simulation and actual data. **a** Forward model. **b** Forward single-shot record. **c**, **d** Actual data dispersion curve and simulated data dispersion curve. **e**, **f** Inversion results of dispersion curves of real and simulated data

(Fig. 9b, white line). The structure of the S-wave velocity showed (Fig. 9b, white line) that the thickness of the sedimentary layer (strongly weathered interface) varies laterally, reaching the deepest thickness of more than 1 km in the Cuona Rift, gradually thinning to the east, where it becomes thicker again at the Jisong fracture. In the eastern Triassic strata, the average sedimentary layer thickness is smaller than that in the western part of Juela Mountain.

The core of the Cuonadong dome is mainly leucogranite, and the S-wave velocity of the slightly weathered granite ranges from 1200 to 2200 m/s based on laboratory data (Ma and Lu 2012; Chen et al. 2021). In this paper, an S-wave velocity greater than 2200 m/s is designated as slightly weathered rock (Fig. 9b, black line). The microweathering interface starts from the middle of the Cuonadong dome, approximately 1 km from the surface, and extends down to 1.2 km in the

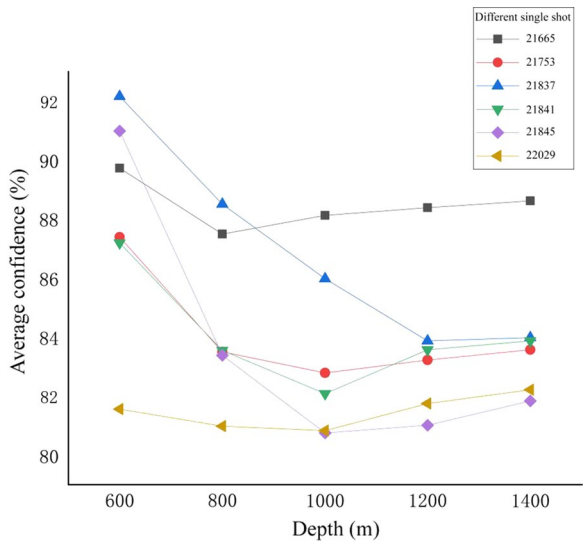

Fig. 7 Average confidence of different depths (21665, 21753, 21837, 21841, 21845, 22029 indicate different points in the profile)

Jisong fracture. There is an anomalous bump (below the red star) approximately 500 m from the surface in the Triassic stratigraphy. Several outcrops of gabbro are present to the east of the profile, and gabbro is a basal shallow-forming intrusive rock with a relatively high density and high velocity. Therefore, we inferred that the anomalous convexity of the eastern microweathered interface may be an intrusive gabbro with high S-wave velocity. By defining the degree of weathering of the rock body in the Cuonadong dome, we infer that the degree of weathering of the rock in the middle and western parts of the dome is higher than that in the east.

Hidden fault

The formation of the Cuonadong dome was influenced not only by east–west and north–south detachment, but also by the intrusion of multiple phases of magma, and the surface cover was severely damaged. At present, several faults have been found around the dome, and they control its structural form. For example, the surface of the Cuona fault in the western part of the profile is covered with Quaternary sediments. The S-wave velocity profile shows (Fig. 9b) that the velocity is less than 1400 m/s, and the dip angle is relatively large. The Jisong fault shows a banded low-velocity body, which can extend down to 800 m. These two main faults are well reflected in the S-wave velocity profile. We inferred that there may be several hidden secondary faults inside the Cuonadong dome via S-wave velocity imaging combined with magnetotelluric data (Jiao et al. 2019) (Fig. 9b, black dashed line). In previous studies, Hyslop surmised that there will be a reflected surface wave in the single-shot record near the fault (Fig. 8b). We also found a reflected surface wave signal on a single-shot record (Fig. 8a) east of the Cuona fault (Fig. 1, black star: 21417), which also indicates that there are some hidden faults at the edge of the Cuonadong dome.

The S-wave velocity profile shows that these secondary faults are mostly located between high and low speeds, and the extension depth is shallow, basically within 1 km. The magnetotelluric results (Fig. 9c) also showed that there are multiple secondary faults in the core of the Cuonadong dome, mainly in the position between high and low resistances (Jiao et al. 2019), which can be well correlated with the S-wave velocity profile. Therefore, through the S-wave velocity profile and electromagnetic profile, we inferred that there are several hidden secondary faults in the core of the Cuonadong dome, which

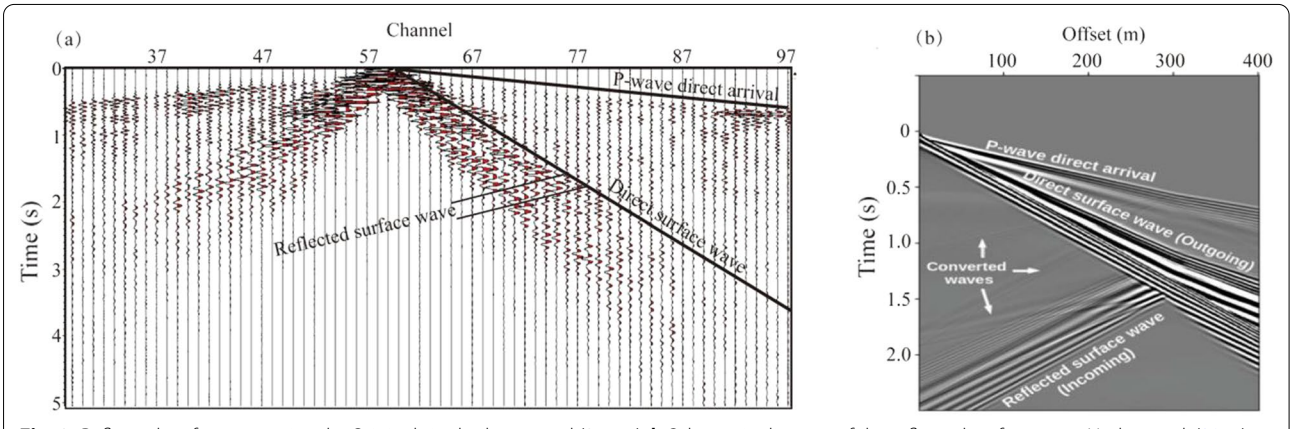

Fig. 8 Reflected surface wave signal **a** Original single shot record (21417). **b** Schematic diagram of the reflected surface wave Hyslop et al. (2015)

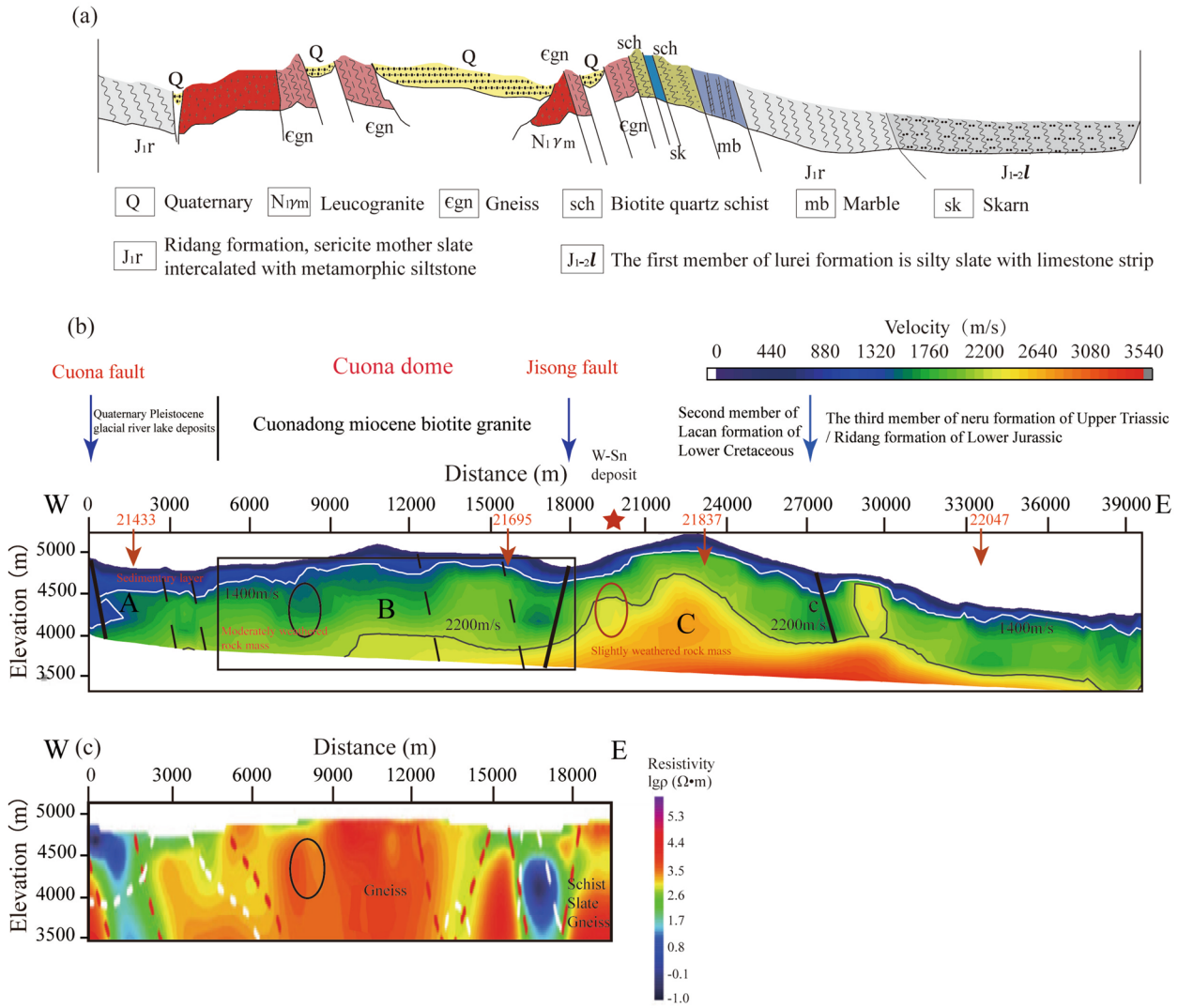

Fig. 9 Comprehensive interpretation of the S-wave velocity profile of the Cuonadong dome. **a** Geologic section. **b** S-wave velocity profile and **c** magnetotelluric profile modified according to Jiao et al. 2019

have larger dip angles, shallow extension depths, and low velocities.

S-wave velocity anomaly and mineralization

The S-wave velocity profiles show that there are three important velocity anomaly regions, reflecting the velocity–field characteristics of different geological structures. Region A includes the Quaternary Pleistocene glacial river and lake sedimentation, and significant lower S-wave velocities, especially in the direction of the Cuona fault, can extend to 1 km. The low-velocity layer to the east gradually becomes shallow, which reflects the spatial morphology of the east–west characteristics of the Cuona fault. Region B is the core of the Cuonadong dome (Fig. 9b, black square) and has a large variety of horizontal S-wave velocities, and the overall high-velocity characteristics are mainly due to the intrusion of Miocene leucogranite, which destroyed the surface cover and caused the horizontal S-wave velocity to vary widely. From the morphology of the high-velocity region, we find that the intrusive body of leucogranite in the Cuonadong dome is low in the west and high in the east. Region C, which is the edge area of the Cuonadong dome, is mainly composed of Cambrian granitic gneiss, Permian schist, Triassic sandstone and slate, and Jurassic cordierite slate. These metamorphic rocks are important metallogenic rocks. The profile passes through a tungsten–tin ore at 20 km (Fig. 9b, red star). The S-wave velocity profile

shows that there is a high-speed abnormal uplift below it (Fig. 9b, red circle), the velocity is significantly higher than that of leucogranite in the core of the Cuonadong dome, and the weathering degree is relatively low. These characteristics may occur because the deep thermal matter rises to the shallow surface along the channel of the Jisong fault, interacts with the surrounding rock, and forms important metallic minerals.

Conclusion

According to the S-wave velocity profile and combined with geological and geophysical data, we revealed the shallow S-wave velocity variations and tectonic characteristics of the Cuonadong dome and adjacent areas and obtained the thickness variations in the sedimentary layers of the dome, the bedrock interface undulation characteristics, the location and extension depth of the hidden secondary fault, and the relationship between shear wave velocity variation and metal deposits:

1. The thickness of the Cuonadong dome sediment layer varies greatly from east to west. The thickness of the sediment layer is the deepest near the Cuona fault and Jisong fault, at more than 1 km, and the core of the dome is the thinnest. The weathering degree of rocks west of the Cuonadong dome is higher than that in the east. The slightly weathered interface in the middle of the dome is approximately 1 km from the surface, the Jisong fault extends downward for 1.2 km, and Juela Mountain is only approximately 500 m.
2. There are many secondary faults in the study area. The depth of the Cuona fault exceeds 1 km, and the Jisong fault is distributed in a band. There are several hidden secondary faults in the core of the Cuonadong dome, which are shallow and may be related to later tectonic movement.
3. Surface wave imaging reveals S-wave velocity characteristics in the Cuonadong dome and its adjacent areas, with obvious high-velocity anomalies below the Cuonadong dome and large horizontal S-wave velocity fluctuations, which are mainly related to the destruction of magmatic activities since the Miocene. The basement is mainly leucogranite, showing low western and high eastern intrusion characteristics. The tungsten tin deposit near the Jisong fault shows an obvious high-velocity anomaly, which may be a channel for deep hydrothermal fluids to intrude upward along the Jisong fault and interact with the surrounding rocks to form metal deposits.

Abbreviations

STDS: Southern Tibetan detachment system; S-wave velocity: Shear wave velocity; W-Sn: Tungsten and tin ore; ITSZ: Yajiang suture zone.

Acknowledgements

We thank all those who helped collect the data and provided project support, especially Sinopec Geophysical Company. We thank associate researcher Li Hongqiang of the Chinese Academy of Geological Sciences (CAGS) for providing the processing software. Finally, we would like to thank all reviewers for their valuable comments on the article.

Author contributions

All authors were involved with the work. GW helped collect the data, processed, analyzed, and interpreted the data, and prepared the manuscript. ZL helped collect the data and assisted with interpretation. HW reviewed and completed the manuscript. SX and WL provided project funding support for this work. YC participated in the preparation of the first draft. SC and WC helped collect the data. All authors read and approved the final manuscript.

Funding

This work is supported by the National Natural Science Foundation of China (Grant Nos. 91962109, 42174124 and 42174094) and the Geological Survey Project of the China Geological Survey (Grant no. DD20221647).

Availability of data and materials

The datasets used and/or analyzed during the current study are available from the corresponding author upon reasonable request.

Declarations

Competing interests

No competing interests.

Author details

[1]Lithosphere Research Center, Institute of Geology, Chinese Academy of Geological Sciences, 26 Baiwanzhuang street, Xicheng District, Beijing 100037, China. [2]Key Laboratory of Deep-Earth Dynamics of Ministry of Natural Resources, Beijing 100037, China.

Received: 10 March 2022 Accepted: 21 July 2022
Published online: 09 August 2022

References

Beaumont C, Jamieson RA, Nguyen MH, Lee B (2001) Himalayan tectonics is explained by the extrusion of a low-viscosity crustal channel coupled to focused surface denudation. Nature 414(6865):738–742. https://doi.org/10.1038/414738a

Blisniuk PM, Hacker BR, Glodny J, Ratschbacher L, Bi S, Wu Z, Calvert A (2001) Normal faulting in central Tibet since at least 13.5 Myr ago. Nature 412(6847):628–632. https://doi.org/10.1038/35088045

Cao HW, Li GM, Zhang Z, Zhang LK, Dong SL, Xia XB, Zhang YH (2020) Miocene Sn polymetallic mineralization in the Tethyan Himalaya, southeastern Tibet: a case study of the Cuonadong deposit. Ore Geol Rev 119:103403. https://doi.org/10.1016/j.oregeorev.2020.103403

Chen Z, Liu Y, Hodges KV, Burchfiel BC, Royden LH, Deng C (1990) The Kangmar Dome: a metamorphic core complex in Southern Xizang (Tibet). Science 250(4987):1552–1556. https://doi.org/10.1126/science.250.4987.1552

Chen JW, Zhao DD, Zong QB, Zhang BS, Di BY, Zhu HB, Wang JL (2021) High precision microtremor technology based on linear array and its application to the fine division of lithostratigraphy. Geophys Geochem Explor 45(02):536–545. https://doi.org/10.11720/wtyht.2021.1418

Dong L, Li GM, Huang Y, Li YX, Cao HW, Zhang Z (2018) Geochemical characteristics, chronology and tectonic significance of the granitic gneiss in the

Yardoi dome, southern Tibet. Miner Pet 38(04):76–87. https://doi.org/10.19719/j.cnki.1001-6872.2018.04.10
Fan WX, Li GM, Jiao YJ, Liang SX (2019) Enlightenment of the characteristics of gravity and magnetic field on the tectonic framework and metallogenesis of the Zhaxikang ore-concentrating area, Tibet. J Jilin Univ Earth Sci Ed. 49(06):1741–1754. https://doi.org/10.13278/j.cnki.jjuese.20190018
Feng HW, Yan WH, Yan S, Guo YX, Hui SX, Chang C (2019) Joint inversion of ambient noise and surface wave for S-wave velocity of the crust and uppermost mantle beneath weihe basin and its adjacent area. Seismol Geol 41(05):1185–1205
Fu JM, Li GM, Wang GH, Huang Y, Zhang LK, Dong SL, Liang W (2017) First field identification of the Cuonadong dome in southern Tibet: implications for EW extension of the North Himalayan gneiss dome. Int J Earth Sci 106(5):1581–1596. https://doi.org/10.1007/s00531-016-1368-2
Fu JG, Li GM, Wang GH, Huang Y, Zhang LK, Dong SL, Liang W (2018a) Establishment of the North Himalaya double gneiss domes: evidence from field identification of the Cuonadong dome, south Tibet. Geol China 45(04):783–802. https://doi.org/10.12029/gc20180410
Fu JG, Li GM, Wang GH, Zhang LK, Liang W, Zhang Z, Zhang XQ, Huang Y (2018b) Synchronous granite intrusion and E-W extension in the Cuonadong dome, southern Tibet, China: evidence from field observations and thermochronology results. Int J Earth Sci 107(6):2023–2041. https://doi.org/10.1007/s00531-018-1585-y
Fu JG, Li GM, Wang GH, Zhang LK, Liang W, Zhang XQ, Jiao YJ, Dong SL, Huang Y (2020a) Structural analysis of sheath folds and geochronology in the Cuonadong Dome, southern Tibet, China: new constraints on the timing of the South Tibetan detachment system and its relationship to North Himalayan Gneiss Domes. Terra Nova 32(4):300–323. https://doi.org/10.1111/ter.12462
Fu JG, Li GM, Wang GH, Zhang LK, Liang W, Zhang XQ, Jiao YJ, Dong SL (2020b) Syntectonic skarn characteristics and mineralization age of associated Be-W-Sn rare metal deposit in Cuonadong Dome, Southern Tibet, China. J Jilin Univ, Earth Sci Ed. 50(05):1304–1322. https://doi.org/10.13278/j.cnki.jjuese.20190285
Guo J, Jiao YJ, Liang SX (2019a) Electrical variation of Carbonaceous rocks in ore-bearing fault zone and its prospecting significance, in Zhaxikang Pb-Zn-Sb polymetallic ore deposit, Tibet, China. J Chengdu Univ Technol Sci Technol Ed. 46(04):471–481. https://doi.org/10.3969/j.issn.1671-9727.2019.04.07
Guo J, Li WC, Li GM, Jiao YJ, Liang SX (2019b) Application of multi-scale integrated geophysical method in prospecting prediction of Zhaxikang Pb-Zn-Sb-Au polymetallic deposit. Earth Sci 44(06):2129–2142. https://doi.org/10.3799/dqkx.2018.362
He CT, Qin KZ, Li JX, Zhou QF, Zhao JX, Li GM (2020) Preliminary study on occurrence status of beryllium and genetic mechanism in Cuonadong tungsten-tin-beryllium deposit, eastern Himalaya. Acta Pet Sin 36(12):3593–3621. https://doi.org/10.18654/1000-0569/2020.12.03
Huang CM, Li GM, Zhang Z, Liang W, Huang Y, Zhang LK, Fu JG (2018) Petrogenesis of the Cuonadong leucogranite in South Tibet: constraints from bulk-rock geochemistry and zircon U-Pb dating. Earth Sci Front 25(06):182–195. https://doi.org/10.13745/j.esf.sf.2018.11.2
Hyslop C, Stewart RR (2015) Imaging lateral heterogeneity using reflected surface waves. Geophysics 80(3):69–82. https://doi.org/10.1190/geo2014-0066.1
Ivanov J, Park CB, Miller RD, Xia JH (2005) Analyzing and filtering surface-wave energy by muting shot gathers. J Environ Eng Geophys 10(3):307–322. https://doi.org/10.2113/JEEG10.3.307
Jiao YJ, Liang SX, Guo J, Zhang W, Liao GZ (2016) The geophysical characteristics of ore-hosted strike slip fault and the prospecting direction in Zhaxikang Pb-Zn-Ag deposit, Tibet. Contrib Geol Miner Resour Res 31(03):434–439. https://doi.org/10.6053/j.issn.1001-1412.2016.03.016
Jiao YJ, Huang XR, Li GM, Liang SX, Guo J (2019) Deep structure and mineralization of Zhaxikang ore-concentration area, Southern Tibet: evidence from geophysics. Earth Sci 44(06):2117–2128. https://doi.org/10.3799/dqkx.2018.352
Jiao YJ, Huang XR, Liang SX, Zhang Z, Li GM (2020) Deep structure and prospecting significance of the Cuonadong dome, Tethys Himalaya, China: geophysical constraints. Geol J 56(1):253–264. https://doi.org/10.1002/gj.3962
Lee J, Hacker B, Wang Y (2004) Evolution of North Himalayan Gneiss Domes: structural and metamorphic studies in Mabja Dome, Southern Tibet. J Struct Geol 26(12):2297–2316. https://doi.org/10.1016/j.jsg.2004.02.013
Li HL, Li GM, Zhang Z, Fu JG, Liang SX (2016) Ore-controlling factors and prospecting prediction of Zhaxikang Pb-Zn polymetallic deposit, Southern Tibet. Met Min. https://doi.org/10.3969/j.issn.1001-1250.2016.10.021
Li GM, Zhang LK, Jiao YJ, Xia XB, Dong SL, Fu JG, Liang W, Zhang Z, Wu JY, Dong L, Huang Y (2017a) First discovery and implications of Cuonadong superlarge Be-W-Sn polymetallic deposit in Himalayan metallogenic belt, southern Tibet. Miner Depos 36(04):1003–1008. https://doi.org/10.16111/j.0258-7106.2017.04.014
Li HL, Li GM, Li YX, Dong SL, Qing CS, Fu JG, Liu H, Huang HX (2017b) A study on ore geological characteristics and fluid inclusions of Jienagepu gold deposit in Zhaxikang ore concentration district, Southern Tibet. China. Acta Miner Sin. 37(06):684–696. https://doi.org/10.16461/j.cnki.1000-4734.2017.06.002
Li HL, Li GM, Ding J, Zhang Z, Qing CS, Fu JG, Ling C, Liu YQ (2020a) Genesis of Zhaxikang Pb-Zn polymetallic deposit in southern Tibet: evidence from in Situ S isotopes of sulfides. J Jilin Univ Earth Sci Ed 50(05):1289–1303. https://doi.org/10.13278/j.cnki.jjuese.20190287
Li QS, Gao Y, Wang XB, Zhao JM (2020b) New research progress in geophysics and continental dynamics of the Tibetan Plateau. China J Geophys. 63(03):789–801. https://doi.org/10.6038/cjg2020O0063
Li QL, Zhang H, Lei XD, Li C, Fang H, Guan W, Han YD, Zhao XC (2022) analyses of internal structure of slope using multi-channel transient surface wave exploration and microtremor survey. Geophys Geochem Explor 46(01):258–267. https://doi.org/10.11720/wtyht.2022.2498
Liang W, Li GM, Basang YD, Zhang LK, Fu JG, Huang Y, Zhang Z, Wang YY, Cao HW (2021) Metallogenesis of Himalaya gneiss dome: an example from Cuonadong gneiss dome in Zhaxikang ore concentration area. Miner Dep 40(05):932–948. https://doi.org/10.16111/j.0258-7106.2021.05.003
Lin B, Tang JX, Zheng WB, Leng QF, Lin X, Wang YY, Meng Z, Tang P, Ding S, Xu YF, Yuan M (2016) Geochemical characteristics, age and genesis of Cuonadong leucogranite, Tibet. Acta Pet Miner 35(03):391–406. https://doi.org/10.3969/j.issn.1000-6524.2016.03.002
Liu GF, Liu Y, Meng XH, Liu LB, Su WJ, Wang YZ, Zhang ZF (2021) Surface wave and body wave imaging of passive seismic exploration in shallow coverage area application of Inner Mongolia. China J Geophys. 64(03):937–948. https://doi.org/10.6038/cjg2021O0064
Ma HY, Lu ZD (2012) Investigation of physico-mechanical properties for highly weathered granite of nuclear power station in coastal site of western Guangdong province. Rock Soil Mech. 33(02):361–366. https://doi.org/10.16285/j.rsm.2012.02.006
Park CB, Miller RD, Xia JH (1998) Imaging dispersion curves of surface waves on multi-channel record. SEG Tech Progr Expand. https://doi.org/10.1190/1.1820161
Park CB, Miller RD, Xia J (1999) Multichannel analysis of surface waves. Geophysics 64(3):800–808. https://doi.org/10.1190/1.1444590
Shi DN, Klemperer SL, Shi JY, Zhao WJ (2020) Localized foundering of Indian lower crust in the India–Tibet collision zone. Proc Natl Acad Sci 117(40):24742–24747. https://doi.org/10.1073/pnas.2000015117
Wang G, Yi HS, Liu S, Shen JH (2010) The deformation transfer from orogen stage to plateau stage in the central part of Tibetan Plateau during Miocene time and its tectonic mechanism. China J Geophys. 53(06):1384–1398. https://doi.org/10.3969/j.issn.0001-5733.2010.06.017
Wang XX, Zhang JJ, Liu J, Yan SY, Wang JM (2012) Transformation of the tectonic system of the Himalayan orogenic belt in the middle Miocene. Chin Sci Bull 57(33):3162–3172. https://doi.org/10.1360/csb2012-57-33-3162
Wei HX, Cha WF, Feng CL (2014) Analysis of characteristics of seismic section in goaf area. Prog Geophys 29(04):1808–1814. https://doi.org/10.6038/pg20140443
Xia J, Miller RD, Park CB (1999) Estimation of near-surface shear-wave velocity by inversion of Rayleigh waves. Geophysics 64(3):691–700. https://doi.org/10.1190/1.1444578
Xia JH, Gao LL, Pan YD, Shen C, Yin XF (2015) New findings in high-frequency surface wave method. China J Geophys. 58(08):2591–2605. https://doi.org/10.6038/cjg20150801
Xie YL, Yu L, Ying X, Li GM, Liu HF, Li YX, Dong SL, JunjieZhou JJ (2017) Genesis of the Zhaxikang epithermal Pb-Zn-Sb deposit in southern Tibet, China: evidence for a magmatic link. Ore Geol Rev 80:891–909. https://doi.org/10.1016/j.oregeorev.2016.08.007

Xie JJ, Qiu HN, Bai XJ, Zhang WF, Wang Q, Xia XP (2018) Geochronological and geochemical constraints on the Cuonadong leucogranite, eastern Himalaya. Acta Geochim 37(3):347–359. https://doi.org/10.1007/s11631-018-0273-8

Xie L, Tao XY, Wang RC, Wu FY, Liu C, Liu XC, Li XK, Zhang RQ (2019) Highly fractionated leucogranites in the eastern Himalayan Cuonadong dome and related magmatic Be-Nb-Ta and hydrothermal Be-W-Sn mineralization. Lithos 354–355:10528. https://doi.org/10.1016/j.lithos.2019.105286

Xie F, Wang HY, Hou HS, Gao R (2021) Near-surface fine velocity structure in Eastern segment of Central Asian Orogenic belt: revealed by first-arrival wave tomography from deep seismic reflection profile. J Jilin Univ Earth Sci Ed. 51(02):584–596. https://doi.org/10.13278/j.cnki.jjuese.20200016

Xu PF, Shi W, Ling SQ, Guo HL, Li ZH (2012) Mapping spherically weathered "Boulders" using 2D microtremor profiling method: a case study along subway line 7 in Shenzhen. China J Geophys. 55(06):2120–2128. https://doi.org/10.6038/j.issn.0001-5733.2012.06.034

Yang PX, Chen ZW, Ren JW, Zhang J (2011) Activity and segmentation of Gyaring Co fault-zone in central Qingzang plateau. Acta Seismol Sin 33(03):362–372. https://doi.org/10.3969/j.issn.0253-3782.2011.03.009

Zhang Z, Zhang LK, Li GM, Liang W, Xia XB, Fu JG, Dong SL, Ma GT (2017) The Cuonadong Gneiss Dome of North Himalaya: a new member of Gneiss Dome and a new proposition for the ore-controlling role of North Himalaya Gneiss Domes. Acta Geosci Sin 38(05):754–766. https://doi.org/10.3975/cagsb.2017.05.15

Zhang H, Liu ZW, He RZ, Li QL (2020) Near surface shear wave velocity structure inversion using multi-order surface wave dispersion curves constructed from deep seismic reflection data: a real case of deep seismic reflection profile across Bangong-Nujiang suture zone. China J Geophys. 63(12):4410–4430. https://doi.org/10.6038/cjg2020O0116

Zhou Q, Li GM, Xia XB, Wu JY, Lai Y, Li YX, Li YC (2014) Metallogenic model of Zhaxikang lead-zinc polymetallic ore concentration area in southern Tibet. Miner Dep 33(S1):353–354. https://doi.org/10.16111/j.0258-7106.2014.s1.179

Publisher's Note